

Spectral Observables and Gauge Field Couplings in Causal Dynamical Triangulations

Giuseppe Clemente and Massimo D'Elia

Abstract In the first part of this Chapter, we discuss the role of spectral observables, describing possible ways to build them from discretizations of the Laplace–Beltrami operator on triangulations, and how to extract useful geometric information. In the second part, we discuss how to simulate the composite system of gauge fields coupled to CDT for generic groups and dimensions, showing results in some specific case and pointing out current challenges.

1 Introduction

One of the most promising results of pure-gravity CDT in 4D is that it appears to be non-perturbatively renormalizable in a Wilsonian renormalization group sense, i.e. there exist second-order critical points which are candidates for extracting continuous physics (see Chapters 1 and 10 of this Section [1, 2]). However, there is still an urge to identify a possibly complete set of physically meaningful observables to characterize all relevant features of the geometries under investigation.

The approach we followed in this respect is based on *spectral methods*, which are a set of techniques involving the analysis of eigenvalues and eigenvectors of discretizations of the Laplace–Beltrami (LB) operators associated with spaces of functions on a manifold. One of the advantages of the spectral decomposition of the LB operators into eigenvalues and eigenvectors is contained in their hierarchical nature, which allows us to consistently separate large-scale features from short-scale ones; in general, the spectrum of a LB operator on a manifold M identifies a set of

Giuseppe Clemente
Deutsches Elektronen-Synchrotron DESY,
Platanenallee 6, 15738 Zeuthen, e-mail: giuseppe.clemente@desy.de

Massimo D'Elia
Dipartimento di Fisica dell'Università di Pisa and INFN - Sezione di Pisa,
Largo Pontecorvo 3, I-56127 Pisa, Italy. e-mail: massimo.delia@unipi.it

characteristic length scales, as we argue in Section 2, while features like directionality, localization, and all the remaining metrical information can be extracted from eigenvectors, which take the role of waveforms (or diffusion) modes.

Another direction that we investigated in order to extract meaningful physical properties of the system from CDT simulations is the problem of minimally coupling gravity and Yang-Mills gauge fields, possibly including also fermionic matter. Not only this is theoretically important in the search for a complete and self-consistently renormalizable quantum theory of gravity in the continuum, since the composite system could possess different critical properties than the pure-gravity one, but also because this allows an easier connection between the theory and possible phenomenological results from quantum cosmological observations, provided these would be available at some point. In Section 3, we describe the algorithmic strategies that we use to implement this minimal coupling, and the challenges that appear for higher dimensions and gauge groups, both algorithmic and regarding the definition of meaningful observables.

2 Spectral methods

The relationship between the geometric properties of a manifold and the spectral decomposition of its associated Laplace–Beltrami (LB) operators is well known in literature [3, 4, 5], and spectral analysis, i.e. the study of eigenvalues and eigenvectors of relevant operators of the model under study, shows a wide spectrum of applications through science and beyond. In this Section, we first introduce some basics regarding the physical role and interpretation of spectra and eigenvectors, followed by a graph discretization of the LB operator with some toy examples. Then we show some numerical results for CDT and discuss other possible discretizations.

2.1 General properties of spectra and eigenvectors

In order to understand the physical content of the LB spectral decomposition, it is useful to start from the example of diffusion processes, for simplicity on boundaryless manifolds \mathcal{M} (either smooth or piecewise flat, as the ones appearing in dynamical triangulations). On a chart with coordinates \mathbf{x} , and with diffusion time t (which is not a physical time), the heat equation takes the form

$$\partial_t u(\mathbf{x}, t) = D^\mu D_\mu u(\mathbf{x}, t), \quad (1)$$

where D_μ and $-D^\mu D_\mu$ are respectively the covariant derivative and the LB operator on \mathcal{M} . One then can proceed by expanding solutions on the basis of an orthonormal set of LB eigenfunctions $\phi_k(\mathbf{x})$ for each t

$$u(\mathbf{x}, t) = \sum_{k=0}^{\infty} c_k(t) \phi_k(\mathbf{x}), \quad (2)$$

and substitute into Equation (1) to obtain

$$\frac{d}{dt} c_k(t) = -\lambda_k c_k(t) \quad \longrightarrow \quad c_k(t) = c_k(0) e^{-\lambda_k t}, \quad (3)$$

with λ_k the eigenvalues of the LB operator associated to $\phi_k(\mathbf{x})$. The coefficients $c_n(0)$ are fixed by the initial condition $u(\mathbf{x}, 0)$. It is straightforward to show that the L_2 norm (weighted by the metric term $\sqrt{g(\mathbf{x})}$) of $u(\mathbf{x}, t)$ is constant in diffusion time t , so we can interpret a solution with norm 1 as a probability distribution. In the case when one starts the diffusion process from a distribution where all probability is concentrated at one point \mathbf{y} , the fundamental solution to the heat equations

$$G(\mathbf{x}, \mathbf{y}; 0) = \frac{1}{\sqrt{\det(g(\mathbf{x}))}} \delta^d(\mathbf{x} - \mathbf{y}), \quad (4)$$

$$\partial_t G(\mathbf{x}, \mathbf{y}; t) = D_{\mathbf{x}}^2 G(\mathbf{x}, \mathbf{y}; t), \quad (5)$$

is the so-called *heat-kernel*, and it can be written either in terms of spectrum and eigenvectors of the LB operator, or as an early (diffusion) time expansion, for any \mathbf{x} and \mathbf{y} , reads as follows [6]:

$$G(\mathbf{x}, \mathbf{y}; t) = \sum_{k=0}^{\infty} e^{-\lambda_k t} \phi_k(\mathbf{x}) \phi_k(\mathbf{y}) \sim \left[\frac{e^{-d_g^2(\mathbf{x}, \mathbf{y})/4t}}{(4\pi t)^{d/2}} \right] \sum_{n=0}^{\infty} a_n(\mathbf{x}, \mathbf{y}) t^n \quad (6)$$

where we denote by $d_g(\mathbf{x}, \mathbf{y})$ the *geodesic distance* between the points \mathbf{x} and \mathbf{y} . For a d -dimensional flat space, the term in square brackets of Eq. (6) is the only one present, because $a_0(\mathbf{x}, \mathbf{y})$ is the only non-zero term in the series. Furthermore, for non-flat but smooth manifolds, the small t regime probes length scales of the order $d_g(\mathbf{x}, \mathbf{y}) \sim \sqrt{t}$, due to the exponential falloff. This is connected to a property of the spectral version of the heat-kernel, appearing in the left expressions of Eq. (6), which consists in how eigenmodes $\phi_k(\mathbf{x})$ with relatively larger eigenvalues λ_k are exponentially suppressed with respect to smaller eigenvalues. Indeed, this shows a key feature of the spectrum (even more evident if one considers the wave equation): the lowest part of the spectrum is associated to the slowest diffusion modes, while the highest part to the fastest. Since the eigenmodes of the LB operator are also solutions to the wave equation, a direct correspondence can be made between eigenvalues and the (inverse squares of the) wavelengths: in these terms, the lowest part of the spectrum is associated to the longest wavelengths¹ while the highest eigenvalues are associated to the smallest ones, which, being related to the ultraviolet scales, can be neglected in the investigation of continuum physics. Another relevant quantity,

¹ There is a disclaimer on the wave interpretation of eigenmodes: since the typical geometries we consider are random, the eigenmodes often exhibit an Anderson-like localization behavior [7, 8], instead of being long-range.

related to the heat-kernel $G(\mathbf{x}, \mathbf{y}; t)$, is the average *return probability* [9, 10, 11, 12], defined as:

$$P(t) := \frac{1}{\text{Vol}(\mathcal{M})} \int d^d \mathbf{x} \sqrt{\det(g(\mathbf{x}))} G(\mathbf{x}, \mathbf{x}; t), \quad (7)$$

which can be analogously expanded in t as:

$$P(t) = \frac{1}{\text{Vol}(\mathcal{M})} \sum_{k=0}^{\infty} e^{-\lambda_k t} \sim \frac{1}{(4\pi t)^{d/2} \text{Vol}(\mathcal{M})} \sum_{n=0}^{\infty} A_n t^n. \quad (8)$$

The coefficients A_n are related to a useful hierarchy of geometric quantities such as volume ($A_0 = \text{Vol}(\mathcal{M})$), total curvature ($A_1 = \frac{1}{3} \int_{\mathcal{M}} R$), and other diffeomorphism invariant scalars built from contractions of higher powers of the Riemann tensor [6, 13]. On a flat space \mathbb{R}^d , the return probability reduces to a power law behavior $P(t) = (4\pi t)^{-\frac{d}{2}}$ (with all coefficients $A_{i \geq 1} = 0$), as expected from scale-invariance. For a (non-pathologically) curved but smooth manifold of dimension d , the leading diffusion behavior at small diffusion times acts is the same as the one of flat space with the same dimension. Therefore, in the case of a smooth manifold \mathcal{M} , just by using the LB spectrum, or equivalently by the return probabilities of diffusion processes at different diffusion times, it is possible to extract information about the dimension of the space

$$d = -2 \lim_{t \rightarrow 0^+} \frac{d \log P(t)}{d \log t}. \quad (9)$$

The geometries appearing in (C)DT are far from smooth, and that means that a small diffusion time extrapolation as the one shown in Eq. (9) is not really meaningful. However, one is not interested in the ultraviolet behavior, which is the one affected by discretization artifacts, but is sufficient to characterize geometries locally in a mesoscopic sense, i.e. for intermediate scales. Indeed, by universality arguments, the continuum limit behavior should be affected only by relevant operators which are insensitive to the finer details of the regularization. As we show in the next section, it is possible to extend the regime of validity of Eq. (9) up to finite diffusion times (instead of evaluating in the limit $t \rightarrow 0^+$) by defining the so-called *spectral dimension*, which can be evaluated at different diffusion times (or equivalently, length scales).

2.1.1 Weyl's law, spectral dimension and connectivity

Let us consider again a d -dimensional smooth manifold \mathcal{M} without boundaries and with spectrum $\sigma(\mathcal{M})$ of the LB operator. The count of eigenvalues below a spectral radius λ can be written as

$$n(\lambda) \equiv \sum_{\lambda_k \in \sigma(\mathcal{M})} \theta(\lambda - \lambda_k) = \int_0^\lambda \rho(\lambda') d\lambda', \quad (10)$$

where we also defined the spectral density $\rho(\lambda) \equiv \frac{dn}{d\lambda} = \sum_k \delta(\lambda - \lambda_k)$. As clear from its definition in terms of eigenvalues, is possible to write the return probability, shown in Eq. (8), as the Laplace transform of the spectral density $P(t) = \mathcal{L}[\rho(\lambda)](t)$. Likewise, the spectral density can then be written as an inverse Laplace transform of the return probability² $\rho(\lambda) = \mathcal{L}^{-1}[P(t)](\lambda)$ which, due to the leading small diffusion time behavior $P(t) \propto t^{-d/2}$, establishes a connection with another important result of spectral geometry called *Weyl's law* [14, 15], describing the asymptotic behavior of the eigenvalue counts $n(\lambda)$ at large spectral radius λ :

$$n(\lambda) \sim \frac{\omega_d V}{(2\pi)^d} \lambda^{d/2}, \quad (11)$$

where ω_d is the volume of the d -dimensional ball of unit radius and $V \equiv \text{Vol}(\mathcal{M})$ indicates the volume of the manifold. The leading dependence in expression in Eq. (11) can be used to build an alternative definition of the spectral dimension, which we call *effective dimension* [16], as a quantity that is in general running at different energy scales λ :

$$d_{EFF}(\lambda) \equiv 2 \frac{d \log(n/V)}{d \log \lambda}. \quad (12)$$

As mentioned in the previous Section, another definition of dimension, called *spectral dimension* [10, 11, 12], can instead be defined in terms of return probability and diffusion times as an extension of the regime of validity of Eq. (9) to finite diffusion times t , namely:

$$D_S(t) \equiv -2 \frac{d \log P}{d \log t}. \quad (13)$$

It should be evident at this point that the two definitions in Eq. (12) and (13) are intimately connected through Laplace transform, which treats the diffusion time t and eigenvalue “energy” λ as variables dual to each other.

Before showing the results of the application in the CDT case, it is useful to see these definitions in action and get some intuition on their general behavior using some simplified toy examples on discretized geometries, for which the smoothness condition is not available, but where one can nevertheless extract geometric information at the mesoscopic scales.

Let us consider a finite difference discretization of a 3-dimensional torus as a regular cubic lattice, with respectively L_x , L_y and L_z sites along three orthogonal directions. Eigenmodes are periodic plane waves $\phi_{\mathbf{k}}(n_x, n_y, n_z) \propto e^{i(k_x n_x + k_y n_y + k_z n_z)}$ with wave number $\mathbf{k} = (k_x, k_y, k_z)$, where $k_i = 2\pi m_i / L_i$ and m_i integers such that $-L_i/2 < m_i \leq L_i/2$. Using \mathbf{m} , the spectrum can be written as

$$\lambda_{\mathbf{m}} = \sum_{\mu=x,y,z} 4 \sin^2 \left(\frac{\pi m_{\mu}}{L_{\mu}} \right), \quad (14)$$

² This comes from the observation that the inverse Laplace transform of $\frac{1}{t^{\alpha}}$ is $\mathcal{L}^{-1}[t^{-\alpha}](\lambda) = \frac{\lambda^{\alpha-1}}{\Gamma(\alpha)} \theta(\lambda)$ and that $n(\lambda)$ is the integral of $\rho(\lambda)$.

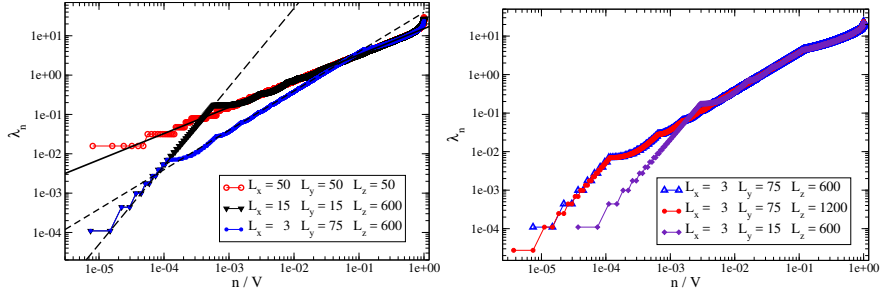


Fig. 1 Plots of λ_n against its volume-normalized order n/V , for a hypercubic lattice with periodic boundary conditions (i.e. toroidal) and different combinations of sizes L_i for each direction. The straight continuous line follows the exact Weyl scaling (see Eq. (11)) expected from a $d = 3$ dimensional space, while the dashed straight lines correspond to effective Weyl scalings for effective dimensions $d = 2$ and 1 , which dominate the largest scale behavior.

but, for our applications, it is more useful to relabel them with a single integer label n and in non-decreasing order $\lambda_{n+1} \geq \lambda_n$. This allows us to use Eq. (12) to extract the effective dimension at different scales from the slope in log-log plots of λ_n versus the *volume-normalized order* $\frac{n}{V}$ (zero-mode excluded). Figure 1 shows, for different combinations of sizes L_i , how there is a quite well-defined scale separation between different eigenvalue ranges with different slopes and therefore different effective dimensions. In particular, notice in the right panel of Figure 1 how the triangle and circle dots, associated with tori which differ only by L_z (and therefore the total volume), exhibit a collapse of their trends and the same slope behavior where transitions between different scaling dimensions happen at the same point in $(\lambda, \frac{n}{V})$, which determines also the smallest eigenvalue, or equivalently, the largest linear size that can be reached. This shows that, using the volume-normalized order $\frac{n}{V}$ instead of just the eigenvalue order label n is essential to compare the spectra from triangulations with different volumes, as we do in Section 2.3.

This example highlights also another important point: since the smallest non-zero eigenvalue, called *spectral gap*, sets the largest length scale of manifolds, it should vanish in the thermodynamical limit, i.e. when the volume diverges. In particular, we expect it to follow a power-law behavior set by

$$\lambda_1 \propto V^{-\frac{2}{d_{EFF,low}}}, \quad (15)$$

where $d_{EFF,low}$ is the effective dimension in the lowest region of the spectrum (large scales). However, in Section 2.3.1 we show that triangulations in the B phase, and some slices in the bifurcation phase C_b possess a gap that does not vanish in the thermodynamical limit. This is related to the observation that geometries in those cases are typically highly connected, and the effective dimension at larger scales is diverging, which is consistent with the relation in Eq. (15). The intimate relation between spectral gap and connectivity can be made more explicit. Indeed, a measure of connectivity for a compact Riemannian manifold \mathcal{M} is encoded in the *Cheeger*

isoperimetric constant $h(\mathcal{M})$, defined as the minimal area of a hypersurface ∂A which bipartitions \mathcal{M} into two disjoint pieces A and $\mathcal{M} \setminus A$ in the most balanced way

$$h(\mathcal{M}) \equiv \inf \frac{\text{Vol}(\partial A)}{\text{Vol}(A) \text{Vol}(\mathcal{M} \setminus A)}, \quad (16)$$

where the infimum is taken over all possible connected submanifolds A . The connectivity, in the form of the Cheeger constant, is bounded by the spectral gap through the *Cheeger inequality* [17]

$$h(\mathcal{M}) \leq 2\sqrt{\lambda_1}. \quad (17)$$

Up to this point, we discussed general properties of spectra without referring to specific discretizations of the LB operator. In the next Section we introduce a graph discretization and show some results of the application of spectral analysis in CDT.

2.2 Graph discretization of the Laplace–Beltrami operator

Here we discuss a specific class of discretizations of the Laplace–Beltrami operator on simplicial manifolds, namely, graph discretizations. In particular, we focus on the discretization as Laplace matrix on the graph dual to the triangulation, where elementary blocks of spacetime volumes, i.e. simplexes, are represented as nodes, while the adjacency relations between them are represented by links. In order to show how this discretization directly connects with functions on the continuous piecewise flat manifold, let us consider a scalar function $f(x)$ on a d -dimensional chart formed by a d -simplex σ_0 and all its adjacent simplexes $\{\sigma_k\}_{k=1,\dots,d+1}$, assuming equilateral lengths of size a for each simplex (Figure 2 illustrates the 2-dimensional case). Since the space inside the chart is flat everywhere, one can Taylor expand around the barycenter \mathbf{x}_0 of σ_0 and with respect to the barycenters $\{\mathbf{x}_k = \mathbf{x}_0 + \delta\mathbf{x}_k\}_{k=1,\dots,d+1}$ of the adjacent simplexes as follows:

$$f(\mathbf{x}_0 + \delta\mathbf{x}_k) = f(\mathbf{x}_0) + \delta x_k^i \partial_i f(\mathbf{x}_0) + \frac{1}{2} \delta x_k^i \partial_i \partial_j f(\mathbf{x}_0) \delta x_k^j + O(|\delta\mathbf{x}_k|^3). \quad (18)$$

In the equilateral case, the magnitude of the displacements $\delta\mathbf{x}_k$ are all proportional to the side lengths a , i.e., $\delta\mathbf{x}_k = \frac{a}{\sqrt{d+1}} \hat{v}_k$ for some unit vectors \hat{v}_k . Furthermore, the unit vectors all sum up to the zero vector $\sum_{k=1}^{d+1} \hat{v}_k = \mathbf{0}$, so one can eliminate the gradient term by summing over all displacements $\delta\mathbf{x}_k$. The best local approximation of the LB operator, using the function evaluation at the barycenters is then given by³

$$-\Delta f(\mathbf{x}_0) = \frac{1}{a^2} \left[(d+1)f(\mathbf{x}_0) - \sum_{k=1}^{d+1} f(\mathbf{x}_k) \right] + O(a), \quad (19)$$

³ Summing over all displacements in the equilateral case results in $\sum_{k=1}^{d+1} \delta x_k^i \delta x_k^j = \frac{a^2}{d+1} \sum_{k=1}^{d+1} v_k^i v_k^j = a^2 \delta_{i,j}$.

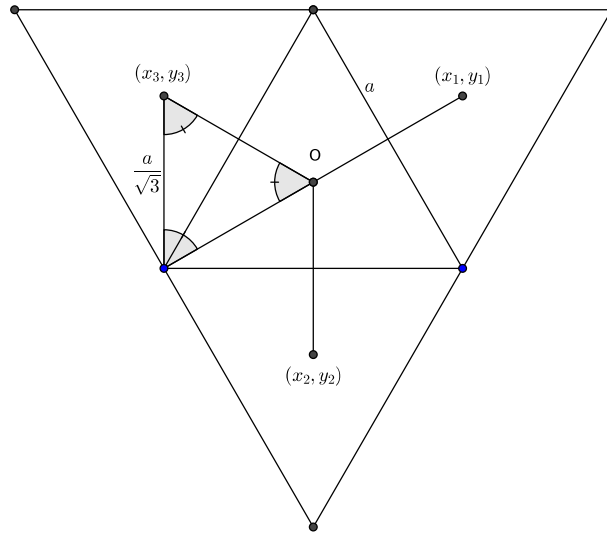


Fig. 2 Sketch of the dual graph discretization of the LB operator in 2D.

In this discretization, the space of scalar functions on the simplicial manifold can then be approximated by the set of values at the barycenter of each simplex $\{p_i\}_{i=0}^{|V|}$, i.e. $\mathbf{f} = (f(p_0), f(p_1), \dots, f(p_{|V|-1})) \in \mathbb{K}$, for some field \mathbb{K} , while the LB operator takes the form of a matrix, called *graph Laplacian*

$$-\Delta \rightarrow L = (d + 1) \cdot \mathbb{1} - A. \quad (20)$$

where A is the adjacency matrix, whose entry A_{ij} is 1 if the simplexes labeled with i and j are adjacent and 0 otherwise.

In the next Section, we show some results of the application of the dual graph Laplacian to investigate the geometric properties of CDT configurations.

2.3 Spectral properties of CDT configurations

In previous sections, we introduced the main tools for spectral analysis. Here we show some qualitative and quantitative results of their application. As discussed in Chapters 1 and 10 of this Section [1, 2], in 4-dimensional CDT there have been identified 4 phases, called A , B , C_{dS} , and C_b . These can be characterized in the first place by their typical volume profiles, i.e. the spatial volume per slice time $V_S(t)$. The A phase is considered unphysical since it exhibits small or absent correlation between adjacent slices, which is not observed in nature. B phase is also considered unphysical, since all space volume is concentrated on a slice. C_{dS} and C_b phases show

instead spatial volumes more distributed in slice time and are therefore appealing for an investigation of the continuum limit, in particular at the transition between C_{dS} and C_b phases, which appears to be second-order [18, 19, 20, 21]. In the rest of this section and the next, we focus on the spectral properties of spatial slices of CDT configurations, since they capture the essential differences between phases, in particular for the C_b phase, discussed separately in Section 2.3.1. As done in Section 2.1.1, we can extract the effective dimension (12) from the slopes of $\lambda, n/V_S$ plots. Figure 3 shows the binned average of the collapsed curves in $(\lambda, \frac{n}{V_S})$ for slices of some typical configurations, while Figure 4 shows their corresponding effective dimension. Notice how the single dominant slice in the B phase configurations

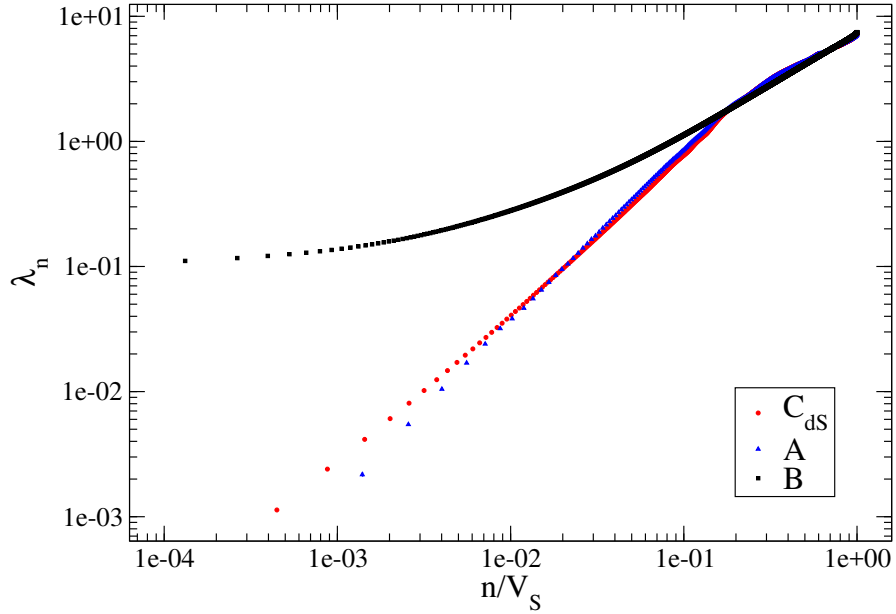


Fig. 3 Averages of λ_n versus n/V_S computed in bins of n/V_S with size $2/V_{S,max}$ for slices taken from configurations sampled deep into the A , B and C_{dS} phases. The volume is fixed to $V_{S,tot} = 40k$ for configurations in A and C_{dS} phase, and to $V_{S,tot} = 8k$ for configurations in B phase. See Ref. [16] for details.

has a diverging effective dimension on long range. As argued in Section 2.1.1, this is related to a gapped spectrum with relatively large λ_1 , associated to a large connectivity of the geometry: since the spectral gap sets the largest scale possible, in B -phase slices, different regions are always quite close to each other, which accounts for the general geometry to be very connected. We are not interested in the properties of A -phase spatial slices, which appear to be vaguely similar to the one of C -phases slices, characterized by an almost constant effective dimension in a wide range of scales and with fractional value (the building blocks are 3-dimensional in this case). The behavior for $n/V_S \gtrsim 0.2-0.5$ should not be taken too seriously, since the

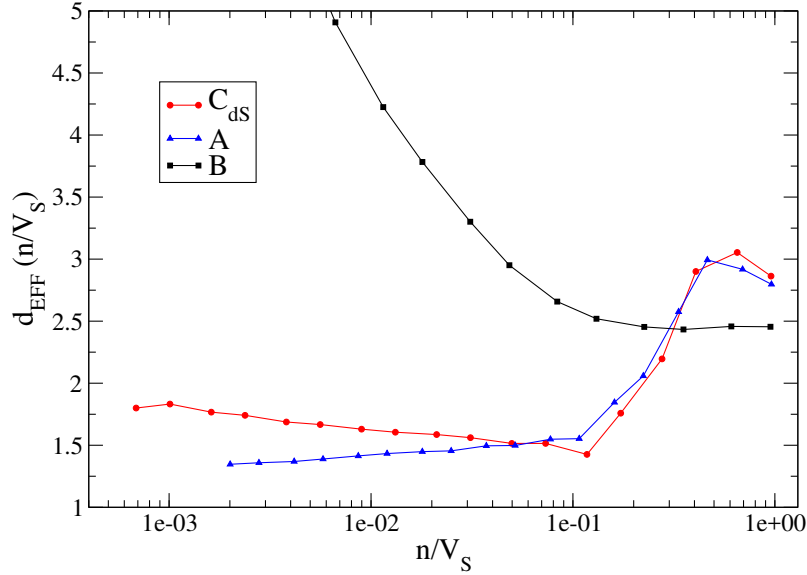


Fig. 4 Running dimension obtained from the logarithmic slope of λ vs $\frac{n}{V_S}$ curves (see Section 2.1.1 and Eq. (12)), computed over windows of different ranges of n/V_S and for configurations sampled in phases C_{dS} , A and B . The curve associated to the B phase is diverging for $n/V_S \rightarrow 0$ (it is around 30 at $n/V_S \sim 10^{-4}$), but part of it has been omitted from the plot, to improve the readability of the curves obtained for the other two phases. See Ref. [16] for details.

corresponding values of λ are already close to the ultraviolet regime (see [16] for more details).

2.3.1 Bifurcation phase and C_b - C_{dS} phase transition

Here we complete the spectral characterization of slice geometries by considering the ensembles of configurations in the bifurcation phase C_b , which exhibits the same typical extended volume profile as the C_{dS} case, but which has been found to differ in the presence of a structure with vertex coordination numbers alternating in slice time between relatively small and large values. From this separation, C_b takes the name “bifurcation” phase. The methods are completely general, but in the following, we always discuss results for spatial slices with spherical topology. From the spectral point of view, Figure 5 shows a qualitative comparison between the average spectral gaps (and a few higher-order eigenvalues) of C_{dS} and C_b slices as a function of the slice time. The alternating structure in slice time is quite noticeable in the slices from configurations in C_b phase, while it does not appear in the ones from C_{dS} phase. Furthermore, it is interesting to notice that for at some scale (around $\lambda \gtrsim \lambda_{100}$ in Figure 5) how the qualitative dependence on the slice time seems to approach

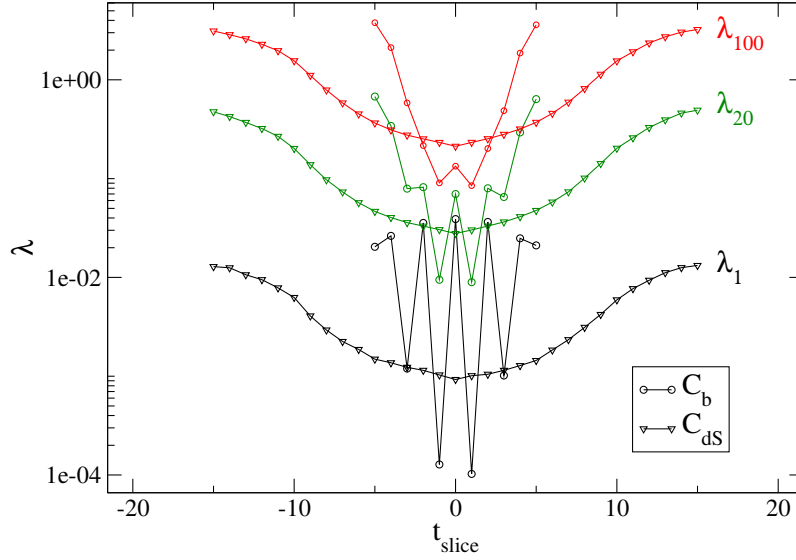


Fig. 5 Averages λ_1, λ_{20} and λ_{100} for configurations in C_b and C_{dS} phases and as a function of the slice-time. The slice-time of maximal slices has been shifted to zero. See Ref. [16] for details.

the C_{dS} one. Since relatively large spectral gaps are associated to highly connected geometries at large scales, as we showed for B -phase slices,

As discussed in Chapters 1 and 10 of this Section [1, 2], it is apparent that C_{dS} and C_b are the only physically relevant phases. Indeed, the average spatial volume distribution observed for ensembles in the C_{dS} phase with spherical slice topology is in good agreement with what is expected from a de Sitter Universe, which corresponds to a S^4 geometry after analytical continuation to the Euclidean space [22]. Unlike C_{dS} , the bifurcation phase C_b is characterized instead by the presence of two different classes of slices that alternate each other in slice time t [20, 21]. This bifurcation behavior of C_b phase is apparent also from the general behavior of the aggregated spectrum of all slices as shown in Fig. 6 for three different values of $\Delta = 0.2, 0.4$ and 0.6 , at the line with constant $k_0 = 0.75$: inside the bifurcation phase, some slices are gapped, but increasing the value of Δ the gap disappears and the two classes of slices merge into a common C_{dS} -like slice behavior. In particular, one can compute the average over an ensemble of configurations at fixed simulation parameters and the infinite volume extrapolation $\langle \lambda_n \rangle_\infty$ for each eigenvalue order n . On the left side vicinity of the critical point, this quantity follows a shifted power law

$$\langle \lambda_n \rangle_\infty = A_n (\Delta - \Delta_c)^{2\nu}, \quad (21)$$

where Δ_c and ν are in general functions of k_0 . Only the coefficients A_n of Eq. (21) depend on the eigenvalue order n , while ν appears to be the same for the lowest orders, with some tension for $n \gtrsim 10$. For example, results of a combined fit with

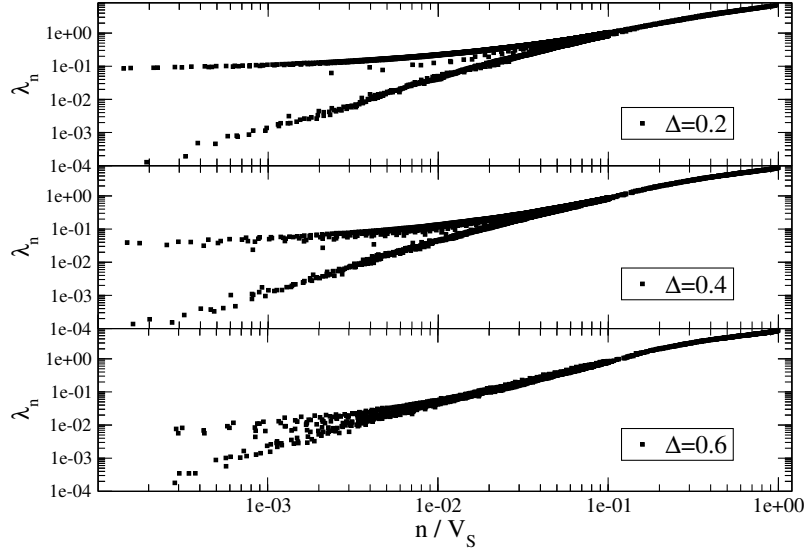


Fig. 6 Scatter plot of λ_n versus n/V_S for the slices (with spatial volume $V_S > 200$) of single configurations sampled at $k_0 = 0.75$, and for three different values of Δ in the C_b phase. See Ref. [16] for details.

Eq. (21), including specifically the orders $n = 1$ and $n = 5$, are shown in Figure 7, and yield $\Delta_c = 0.635(14)$, $\nu = 0.55(4)$ for $k_0 = 0.75$ ($\chi^2/\text{d.o.f.} = 31/26$), and $\Delta_c = 0.544(36)$, $\nu = 0.82(12)$ for $k_0 = 1.50$ ($\chi^2/\text{d.o.f.} = 6/14$). Since eigenvalues at each order n can be interpreted as distinct characteristic long-range lengths, the observation that they appear to scale with the same exponent ν suggests that a single length scale (e.g. the spectral gap λ_1) determines the general scaling behavior at the large length scales. This is reassuring because it is expected to happen when continuum physics behavior, where all quantities can be described by the scaling of a single characteristic length ξ , typically in the form of a correlation length. Therefore gap between C_b and C_{dS} phases closes as expected from a second-order phase transition, and for both the values of k_0 investigated.

2.4 An alternative approach to the Laplacian discretization: Finite Element Methods

The graph discretization of the LB operator is certainly useful, but in general, other discretizations are possible, as well as extensions to the space of vector or tensor fields, as investigated in Ref. [23], where generalized spectral dimensions are defined. Here we introduce a Finite Element discretization as an alternative tool that allows investigating some features not available in general with graph or other discretization

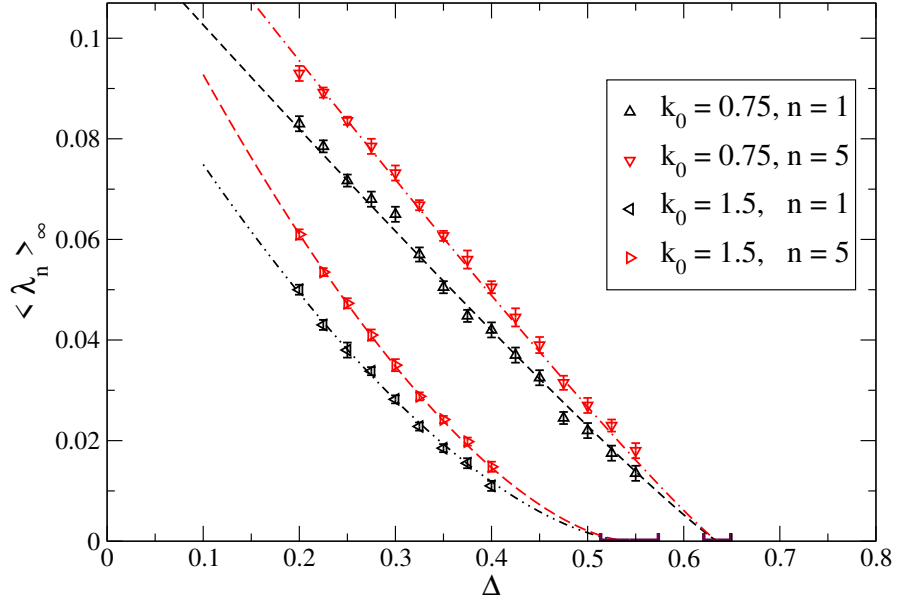


Fig. 7 Critical scaling of the spectral gap and lowest order eigenvalues approaching the C_b - C_{as} phase transition and best fit with Eq. (21).

in a consistent way. This Section is based on Ref. [24], which should be referred to for a more detailed discussion.

2.4.1 Weak formulation and the Finite Element Methods

The name Finite Element Methods (FEM) covers a wide family of approximation techniques that are applied in many fields, where complex modeling is necessary, to numerically solve very general integro-differential equations [25, 26, 27, 28, 29]. As we describe in more detail in the following, the general procedure consists in casting the components of the problem under investigation into simpler and smaller parts, which makes the problem easier to be treated numerically.

In the context of performing spectral analysis of general manifolds FEM consists in casting the LB eigenproblem

$$-\Delta f(\mathbf{x}) = \lambda f(\mathbf{x}). \quad (22)$$

into a weak formulation by multiplying both sides by a test function $\phi(\mathbf{x})$ and integrating everywhere, which results, for a boundaryless manifold \mathcal{M} , in

$$\int_{\mathcal{M}} d^d x \nabla \phi(\mathbf{x}) \nabla f(\mathbf{x}) = \lambda \int_{\mathcal{M}} d^d x \phi(\mathbf{x}) f(\mathbf{x}), \quad (23)$$

where integration by parts has been performed on the left side. The test function ϕ can belong to different classes of functions, but it is customary for the LB eigenproblem to consider the Sobolev space $H^1(\mathcal{M})$, or simply H^1 , defined as the space of L^2 functions that admit weak first derivatives, since the problem is well-posed and solutions are proven to exist. We want to stress that, for a piecewise-linear manifold \mathcal{M} , the Sobolev space $H^1(\mathcal{M})$ involves all functions on the whole domain of the manifold, i.e., not just the vertices or the simplex centers, but also the interior of flat simplexes. In the following, we call the spectrum of the Laplace–Beltrami operator on the space of functions $H^1(\mathcal{M})$ the *exact LB spectrum*. However, this space is infinite-dimensional and cannot be treated numerically, even in the weak form shown in Eq. (23). One then needs to set up an approximation scheme by building a sequence $\{\mathcal{V}_r\}_{r=0}^\infty$ of finite-dimensional subspaces of H^1 with increasing dimension such that in the limit one recovers the full space $\lim_{r \rightarrow \infty} \mathcal{V}_r \rightarrow H^1$. Accordingly, the approximate eigenvectors on $f_n^{(r)}$ and eigenvalues $\lambda_n^{(r)}$ would converge, in the limit $r \rightarrow \infty$ to the exact LB eigenvectors and eigenvalues of the infinite-dimensional problem (23) in H^1 . In practice, chosen a finite set of basis functions $\{\phi_i^{(r)}\}_{i=1, \dots, N_r}$ for the subspace \mathcal{V}_r , any function $f \in H^1$ can be approximated as

$$f(\mathbf{x}) = \sum_{i=1}^N c_i \phi_i(\mathbf{x}). \quad (24)$$

With this expansion, and the basis used as test functions, Eq. (23) can be rewritten in the form of a finite-dimensional generalized eigenvalue problem:

$$L\mathbf{c} = \lambda M\mathbf{c} \quad (25)$$

where we have introduced the two matrices L and M with matrix elements:

$$L_{i,j} \equiv \int_{\mathcal{M}} d^d \mathbf{x} \nabla \phi_i(x) \cdot \nabla \phi_j(x), \quad (26)$$

$$M_{i,j} \equiv \int_{\mathcal{M}} d^d \mathbf{x} \phi_i(x) \phi_j(x). \quad (27)$$

For the specific class of FEM we considered, the procedure of building a consistent sequence of subspaces is called *refinement*, and it allows extrapolating the result of solutions of the approximate LB eigenproblem on a finite set of subspaces \mathcal{V}_r to the infinite *refinement level* r limit, which corresponds to H^1 . The details of this construction and the convergence properties of the extrapolation to infinite refinement level are technical and have been left out of the following discussion, where we assume all results as already extrapolated, but the reader can find a comprehensive discussion in Ref. [24]. The main point of the FEM discretization of the LB operator is actually the fact that it allows one to extract, by extrapolation, an arbitrarily good approximation to the result of the eigenproblem on the full infinite-dimensional Sobolev space of functions H^1 on the piecewise-flat manifold under investigation. Of course, while

powerful, this approach is certainly not numerically cheap. However, we think it is useful in order to check how much results obtained with other discretizations of the LB operator deviate from the exact spectrum and eigenfunctions, as we discuss in the next Section.

2.4.2 Numerical Results

Here we show a comparison between the few smallest eigenvalues of the LB operator acting on the Sobolev space of functions H^1 for CDT slices, accessed through FEM, and the results of the dual graph discretization of the LB operator, as described in Section 2.2. In Ref. [24], a detailed discussion The effective dimension obtained with the two methods is investigated in Ref. [24] for slices in two points in the phase diagram. For example, for $(k_0, \Delta) = (0.75, 0.7)$ the best effective dimension estimate via FEM suggests a value $d_{EFF}^{(FEM)} = 2.088(18)$, which is in contrast with the value $d_{EFF}^{(DG)} \simeq 1.6$ as found in Ref. [16]. For the sake of comparison, we show here how the estimate of the critical index of the C_b - C_{dS} transition along the line $k_0 = 0.75$ differs from the one computed using dual graph methods, which has been discussed in Section 2.3.1.

In order to extract results useful for the continuum limit, the following three limiting procedures should be performed

1. for each simplicial manifold \mathcal{M} , one has to extrapolate the individual FEM eigenvalues to “infinite refinement level” $\lambda_n^{(r)}[\mathcal{M}] \xrightarrow{r \rightarrow \infty} \lambda_n^{(\infty)}[\mathcal{M}]$, in order to obtain an accurate enough approximation of the spectrum of the exact LB differential operator on \mathcal{M} (see Ref. [24] for details about this step);
2. for each ensemble of configurations at specific values of the parameters, one should first perform an average of the eigenvalues at each specific order n and then take the thermodynamic limit (i.e., infinite volumes in lattice units) $\langle \lambda_n \rangle_V \equiv \frac{1}{|C_V|} \sum_{\mathcal{M} \in C_V} \lambda_n^{(\infty)}[\mathcal{M}] \xrightarrow{V \rightarrow \infty} \langle \lambda_n \rangle_\infty$ by considering the spectra of ensembles C_V with increasing volumes;
3. finally, one can study the critical scaling of the twice-extrapolated eigenvalues $\langle \lambda_n \rangle_\infty(k_0, \Delta)$ observed as the phase transition is approached and match it with the shifted power law expressed by Eq. (21).

In the rest of this Section, we considered only some points along the line $k_0 = 0.75$, and the critical scaling of the first ten orders of eigenvalues. First, we have to possibly extrapolate to infinite refinement level, and then we can perform the thermodynamic limit ($V_S \rightarrow \infty$) order by order. For this second step, in general we do not have a precise expectation on the large-scale behavior for the eigenvalues of gapped slices, but we followed [30] and used the simplest form compatible with data, that is, a quadratic polynomial in $1/V_S$:

$$\langle \lambda_n \rangle_V = \langle \lambda_n \rangle_\infty + \frac{A_n}{V_S} + \frac{B_n}{V_S^2}. \quad (28)$$

The thermodynamical limit consists then of fitting data with Eq. (28) in order to extract the possibly non-zero constant terms $\langle \lambda_n \rangle_\infty$, order by order in n . For every

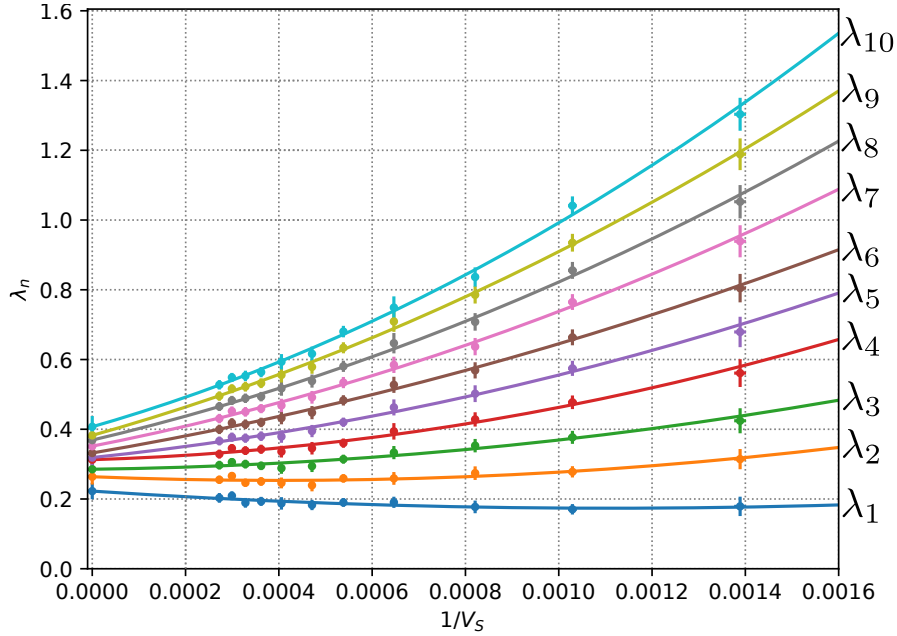


Fig. 8 First ten eigenvalue orders of spatial slices (with $V_S > 500$) vs $1/V_S$, with extrapolation to the thermodynamic limit ($V_S \rightarrow \infty$) in C_b phase. Phase space point $(k_0, \Delta) = (0.75, 0.7)$, total spatial volume $V_{S,tot} = 80k$.

point in the phase diagram and every order n taken into account, the thermodynamic limit extrapolations yielded $\chi^2/dof < 1$. For illustration purposes, Figure 8 displays the extrapolation to the thermodynamic limit for the first ten eigenvalue orders in the phase space point $k_0 = 0.75, \Delta = 0.575$. We then analyzed the first ten eigenvalue orders by fitting our data with the shifted power law in Eq. (21), imposing a common critical index ν and critical point Δ_{crit} for every order n , as observed also for the dual graph case discussed in Section 2.3.1. We used data coming from eight phase space points with Δ ranging from 0.45 to 0.625: we chose not to go too deep inside C_b phase because of the influence of the expected sub-dominant terms of the critical scaling and excluded them by checking the stability of our estimate of ν under the removal of the points with lower Δ parameter. We obtained, as best-fit parameters $\nu = 0.293(10)$ (recall that $\nu^{(DG)} = 0.55(4)$ in Section 2.3.1 at the same value of k_0) and $\Delta_{crit} = 0.6316(15)$, with reduced chi-squared $\frac{\chi^2}{dof} = \frac{67}{68} \simeq 1$. Data and best-fit curves for each order up to $n_{max} = 10$ are displayed in Figure 9.

In conclusion, it is apparent that data are still qualitatively compatible with the critical scaling from dual graph spectra discussed in Section 2.3.1 and based on [30], but, while the location of the transition line agrees with those results, the values found

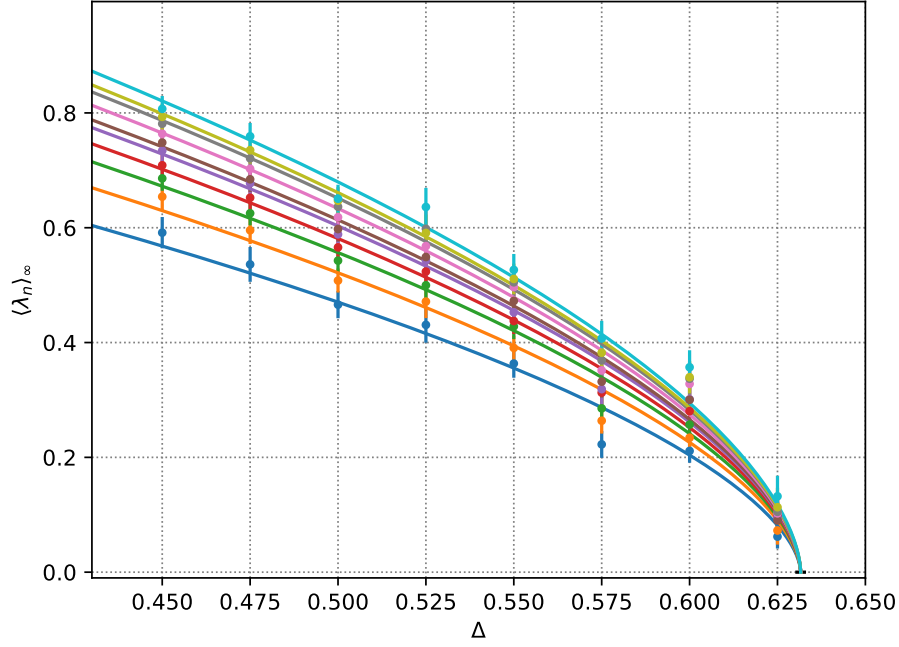


Fig. 9 Critical behavior of the first ten eigenvalue orders along the line at fixed $k_0 = 0.75$ and varying Δ , with best-fit curves of the form shown in Equation (21) with common ν and Δ_{crit} . Curves of increasing eigenvalue order are shown from below to above in the plot.

for the critical indexes appear significantly different than the previous estimates. Such a difference might be important in assessing the quality of estimates based on graph discretization, in particular, if critical indexes of different observables have to be compared to find a physical continuum limit in the phase diagram.

3 Gauge fields on fluctuating geometries

The study of Dynamical Triangulations in the presence of additional quantum fields has been considered frequently in the literature. This is quite natural: if CDT will reveal a successful way to quantize QG, it should eventually be considered in connection with other interacting fields; on the other hand, the presence of other fields may by itself enter the analysis of the renormalization group flow and the search for the continuum limit.

Abelian and non-Abelian gauge fields are a notable case, given their role in the formulation of the standard model. A first important aspect concerns the way the local gauge symmetry and the gauge fields are implemented in the context of Dynamical Triangulations. Gauge fields in a discrete setting, e.g., a hypercubic lattice, are usually described [32] in terms of elementary parallel transporters living on lattice

links (gauge link variables), which permit to *translate* the local frame choice for the internal symmetry group from one lattice site to the other. Therefore, local gauge transformations act on lattice sites, which is the same place where matter fields live.

In the context of Dynamical Triangulations, it is most natural instead to make the choice for the internal symmetry consistent with that for the Lorentz symmetry, i.e. to associate gauge transformations to the simplices composing the triangulations. In this way, the elementary parallel transports are associated with the links of the dual graph, which connect adjacent simplices and are dual to the hypersurfaces separating them.

Once the nature of gauge transformations and gauge fields on the triangulation has been clarified, the first task is to write down a properly discretized action for the composite gravity-gauge system. In the following, $C_G(\mathcal{T})$ will stand for the space of all possible gauge field configurations on the triangulation \mathcal{T} , where G is the gauge group. The action can be formally decomposed, in the minimal coupling paradigm, as $S[\Phi, \mathcal{T}] = S_{CDT}[\mathcal{T}] + S_{YM}[\Phi; \mathcal{T}]$, with $\Phi \in C_G(\mathcal{T})$ and where S_{YM} represents the minimally coupled gauge action in the gravity background \mathcal{T} . The specific form of S_{YM} , which correctly represents Yang-Mills theory in the continuum limit, can be easily built taking as a guide what is usually done on a standard hypercubic lattice [32], as we discuss in more detail in the following.

3.1 Yang-Mills action coupled to Dynamical Triangulations

Continuum Yang-Mills (YM) theories are described in terms of the gauge field $A_\mu = A_\mu^a T^a$, where T^a are the generators of the Lie algebra ($a \in \{1, \dots, N^2 - 1\}$ for $SU(N)$, normalized as $\text{Tr}(T_a T_b) = \delta_{ab}/2$), while the continuum action in flat Euclidean space reads

$$S_{YM} = \frac{1}{4} \int_{\mathcal{M}} d^d x F_{\mu\nu}^a F^{a\mu\nu}, \quad (29)$$

where $F_{\mu\nu}^a = \partial_\mu A_\nu^a - \partial_\nu A_\mu^a + g f^{abc} A_\mu^b A_\nu^c$. A minimal coupling to gravity (described in terms of the Einstein-Hilbert action) leads to the following modification:

$$S_{YM+EH} = \int_{\mathcal{M}} d^d x \sqrt{-g} \left[\frac{1}{4} F_{\mu\nu}^a F^{a\mu\nu} + (R - 2\Lambda) \right], \quad (30)$$

where g in $\sqrt{-g}$ stands now for the determinant of the metric tensor, R is the scalar curvature and Λ the cosmological constant.

In flat space-time, YM theories are usually discretized on a hyper-cubic lattice in terms of link variables $U_\mu(n)$, representing the elementary parallel transporters from lattice site n to lattice site $n + \hat{\mu}$ and taking values in the gauge group G . Local gauge transformations $g(n)$ act on lattice sites, and gauge link variables transform as $U_\mu(n) \rightarrow g(n) U_\mu(n) g^{-1}(n + \hat{\mu})$. The standard and simplest gauge invariant discretization of the action is given in terms of the so-called *plaquette* operator

(plaquette or Wilson action):

$$S_{\text{YM}} \equiv -\frac{2N}{g^2} \sum_{\square} \left[\frac{1}{N} \text{ReTr} \Pi_{\square} - 1 \right], \quad (31)$$

where Π_{\square} stands for the oriented product of gauge link variables around an elementary plaquette \square , and the sum extends over all possible plaquettes⁴. The fact that Eq. (31) correctly reproduces continuum YM in the naïve continuum limit follows from the second order expansion of the correspondence between plaquettes and continuum field strengths, $\Pi_{\mu\nu} \simeq \exp(iga^2 F_{\mu\nu})$, where $\mu\nu$ fixes the plaquette orientations and a is the lattice spacing, which in turn derives from the correspondence $U_{\mu} \simeq \exp(igaA_{\mu})$.

On a triangulated, curved space-time instead, as already explained above, we consider a formulation where elementary parallel transporters are associated with dual links connecting pairs of adjacent simplices. In the following, such variables will be indicated as $U_{\mu}(s)$, where s stands for a particular simplex and μ is the dual link direction, or simply as U_l , where l is the dual link joining two simplices s and s' ; under a local gauge transformation $g(s)$, $U_l \rightarrow g(s)U_l g^{-1}(s')$. All dual links connect ideally the centers of the simplices, so they all have equal lengths, except when simplices are anisotropic, as usual in 4D CDT. Gauge invariant objects are associated with traces of closed loops over the dual graph and, in analogy with the standard formulation, we will call *plaquette* the most elementary closed loop, as well as the gauge invariant operator associated with it. A plaquette encloses an elementary 2D surface of the dual graph, which is dual to a $(d-2)$ simplex of the original triangulation, i.e. a *bone* in the Regge terminology [33]: this is the geometrical object where space-time curvature resides, now it becomes the object where the *gauge curvature* lives as well.

A plaquette Π_b corresponds to the ordered product of n_b dual link variables going around bone b , where n_b is the coordination number of the bone. The area enclosed by an elementary plaquette is An_b , where A is the elementary unit of area (e.g., one third of the simplex area in two dimensions), so that the correspondence between plaquettes and continuum field strengths reads:

$$\Pi_b \simeq \exp(ign_b A F_{\mu\nu}) \quad (32)$$

where μ and ν define the plane orthogonal to the bone. The second order expansion of the trace of the plaquette returns $F_{\mu\nu}^2$, also in this case, however accompanied by a factor n_b^2 which, contrary to what happens on a lattice with a fixed and homogeneous geometry, is a dynamical variable that must be properly taken care of.

In order to understand how, let us consider that, in the continuum action, $F_{\mu\nu}^2$ gets multiplied by $d^d x \sqrt{-g}$ factor, which measures the physical volume. If we want to count volume while summing over bones, we have to take into account the volume pertaining to each bone, which is proportional (times a constant geometrical factor for isotropic simplices) to the number of simplices sharing the bone, i.e. to the

⁴ For the Abelian gauge group $U(1)$, the factor $2N/g^2$ is substituted by $1/g^2$.

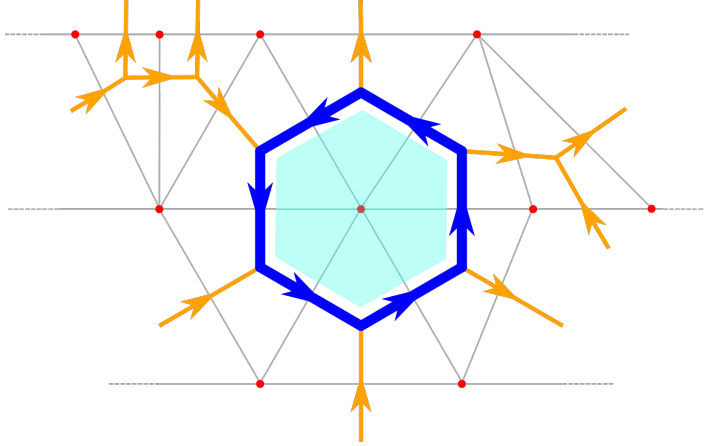


Fig. 10 Sketch of a plaquette operator on a typical 2D CDT triangulation. We have considered a plaquette built around a vertex with $n_b = 6$, corresponding to zero curvature. The direction of gauge links (apart from those belonging to the plaquette) has been drawn according to the convention adopted in the text, i.e. from bottom to up and from left to right. All triangles in this and the following figures should be considered as equilateral, even if they are necessarily drawn differently.

coordination number n_b . From this reasoning it is clear that, since the second order expansion of the plaquette returns $F_{\mu\nu}^2$ with a n_b^2 factor attached, one needs to divide by n_b the contribution from each plaquette and then sum over all plaquettes. The form of the plaquette action over a triangulation \mathcal{T} then reads:

$$S_{\text{YM}} \equiv -\beta \sum_{b \in \mathcal{T}^{(d-2)}} \frac{\tilde{\Pi}_b}{n_b}, \quad (33)$$

where we adopted the shorthand $\tilde{\Pi}_b \equiv [\frac{1}{N} \text{ReTr} \Pi_b - 1]$, $\mathcal{T}^{(d-2)}$ is the set of all bones of the triangulation \mathcal{T} , while β denotes, as usual, the inverse gauge coupling proportional to $1/g^2$. This expression is valid for any dimension d , however the exact definition of β includes geometrical factors (like the elementary area A and the simplex volume) which depend on d .

In the following, we will consider an explicit realization of the above formulation in two space-time dimensions. In this case the gravity sector becomes particularly simple: the curvature term depends only on the global topology of the manifold (Gauss-Bonnet theorem), which is usually kept fixed, so it can be ignored and the cosmological constant term is the only non-trivial coupling. In particular, the pure-gravity contribution for CDT action in Euclidean space-time reads [34]:

$$S_{\text{CDT}}^{(2D)}[\mathcal{T}] = \lambda N_2[\mathcal{T}], \quad (34)$$

where $N_2[\mathcal{T}]$ is the number of simplices (triangles) in \mathcal{T} and λ is the only coupling, related to the cosmological constant. When considering the integral over all possible triangulations weighted by $\exp(-S_{\text{CDT}}^{(2D)}[\mathcal{T}])$, a critical behavior is observed as $\lambda \rightarrow \lambda_c = \log 2$; in particular, both the average total volume and the correlation length for foliation volumes diverge as $\lambda \rightarrow \lambda_c$ from above.

In Fig. 10 we show an explicit realization of a configuration of gauge link variables $U_\mu(s)$ living on a 2D causal triangulation, and of a plaquette built with them. In this case μ is either spatial or temporal, with positive orientations taken rightward in space and upward in time; each simplex is associated with one temporal link (either ingoing or outgoing) and two spatial links (one ingoing and one outgoing). In the particular example of plaquette shown in the figure, we have $n_b = 6$, which corresponds to a locally flat space-time (while $n_b > 6$ and $n_b < 6$ correspond, respectively, to negative and positive local curvature).

3.2 Numerical simulations of CDT coupled to YM theories

A Monte-Carlo approach to the computation of path-integral averages requires to sample the possible triangulation+gauge field configurations according to their weight, $\exp(-S_{\text{CDT}}^{(2D)} - S_{\text{YM}})$, with S_{YM} defined in Eq. (33). In order to that, one has to devise a set of Markov chain moves which guarantee detailed balance, ergodicity and aperiodicity. Since the action is local, the natural choice is to look for a set of local moves, which change the triangulation and/or the gauge configuration only locally. Moreover, it seems convenient to think of moves which change alternatively either the gauge field or the triangulation, so that one can try to implement standard algorithms already used either for lattice gauge theories or for CDT.

However, while this idea works smoothly for updating gauge configurations, moves regarding the triangulation present some additional difficulties. Indeed, any change in the space-time geometry modifies the gauge connection as well: some simplices are added/destroyed or differently glued with the rest of the triangulation, implying a modification of the dual graph and of the gauge link variables living on it. Therefore, one can refer to standard CDT moves (for a review, see Ref. [34]), however a proper modification must be devised, involving a certain number of gauge links which are added/destroyed or differently connected with the rest of the gauge configuration: as the number of space-time dimensions increases, the number of link variables involved in each CDT move increases, making the task less and less trivial. Partial local gauge fixing can help reducing the number of non-trivial link variables involved, and in fact permits to construct a viable algorithm in two dimensions, which is the case more deeply discussed in the following.

3.2.1 Algorithm for 2D CDT

The algorithm usually adopted in pure gravity CDT simulations is a local Metropolis–Hastings⁵ algorithm [35, 36], based on a set of moves that need to preserve the causal structure of the triangulation, i.e. that change the triangulation without spoiling its foliation; a proper set is provided by the so-called Alexander moves [37, 38]. In two dimensions, the set consists of just three moves, usually denoted as (2, 2), (2, 4) and (4, 2), to specify the number of simplices involved before and after the move. In the following, we provide a brief description of such moves and discuss how they must be modified in order to take into account the corresponding modification of the gauge configuration. A more detailed discussion and a proof of detailed balance for the modified moves can be found in Ref. [39]. However, before doing that, we describe the Markov chain steps implemented to modify the gauge field configuration at fixed triangulation, which is a standard extension of the heat-bath algorithms usually adopted in lattice gauge theories.

Pure gauge move - This is similar to what generally implemented in standard lattice gauge theories, and is based on the probability distribution for a given gauge link variable U_l (l is a link of the dual lattice), which stems from Eq. (33) for fixed values of the other gauge link variables:

$$P(U_l)dU_l \propto dU_l \exp\left(\frac{\beta}{N} \text{Re Tr} \left[U_l F_l^\dagger \right]\right). \quad (35)$$

In Eq. (35) dU_l stands for the gauge invariant Haar measure over the gauge group, while F_l is the so-called local *force* acting on that link, $F_l \equiv \sum_{b \ni l} (X_b^{(l)} / n_b)$ where $X_b^{(l)}$ is the *staple* going around the bone b , i.e. the ordered product of the other links that form one of the plaquettes containing l (in particular that going around bone b). In general, one can identify 2 such bones in two dimensions, 3 in three dimensions, 4 in four dimensions and so on; in Figure 11 we sketch such construction for the two-dimensional case, where the convention chosen for the direction of multiplication of the gauge links around the staple is also clarified. We notice that, once the force F_l has been defined, the probability distribution in Eq. (35) is identical to what found in standard lattice gauge theories.

The local algorithm then proceeds by selecting randomly a dual link l randomly and by updating the corresponding variable U_l . This can be done by a standard heat-bath algorithm [40, 41], i.e. by drawing a new gauge link variable U'_l , in place of U_l , according to the distribution in Eq. (35); the Cabibbo-Marinari algorithm [42] can be also easily implemented for $N > 2$, and microcanonical (over-relaxation) steps

⁵ It is interesting to notice that Dynamical Triangulations is one of the cases where the Hastings variant of the original Metropolis algorithm is actually needed. Indeed, since the move modifies the space of stochastic variables, selection probabilities for the move and for its inverse in general differ, so that their ratio contributes to the acceptance step.

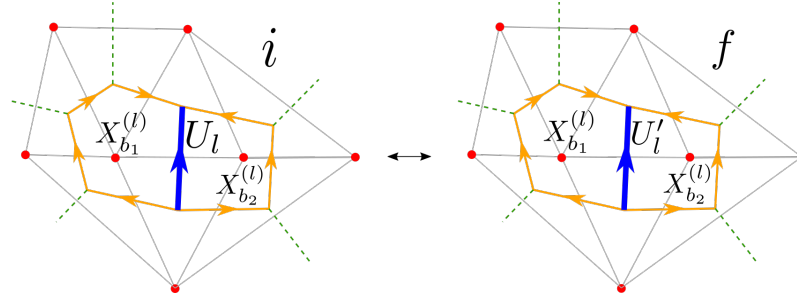


Fig. 11 Sketch of a typical pure gauge move on a two-dimensional causal triangulation, where a single link variable is changed, living on the dual link l (in blue). Here and in the following, the left and right figures indicate respectively the initial (i) state and the final (f) one. The orientation of the products of gauge links making up the two staples $X_{b_1}^{(l)}$ and $X_{b_2}^{(l)}$ is indicated by the arrows (orange paths).

can be alternated to improve efficiency.

Triangulation move (2, 2) - This move consists in flipping a time-like edge of the triangulation, hence the link dual to it, as sketched in Figure 12. The total number of simplices is left unchanged, so the pure gravity part of the action is untouched, however the move changes the space $C_G(\mathcal{T})$ of the gauge configurations. In particular, the coordination number n_1 , n_2 , n_3 and n_4 of the four plaquettes appearing in the figure is changed by one unit (plus or minus), and the gauge variable living on the flipped link enters such plaquettes in a different way.

An easy way to proceed is to exploit gauge invariance and consider that the Markov move can be viewed as acting from any of the configurations which are gauge equivalent to the starting one, to any of the configurations which are gauge equivalent to the final one, i.e. as a move between two different gauge equivalence classes (orbits). Therefore, by a proper gauge transformation, one can always choose the starting and final configurations such that the gauge variable living on the flipped link is gauge fixed to the identity in both cases: in practice, that means applying a partial gauge fixing before the move is performed. In this way, the four plaquettes involved in the move, $\Pi_{1 \leq i \leq 4}$, are left unchanged, even if the gauge action changes anyway, because of the modification in the coordination numbers, however this is easily taken into account by the Metropolis-Hastings acceptance step.

Triangulation (2, 4)-(4, 2) moves - These moves, which are the inverse of each other, are sketched in Figure 13. They are more involved than the (2, 2) one. They change the volume of the triangulation, creating or eliminating two simplices and a vertex of coordination four, so that the pure gravity action changes by $\Delta S_{CDT}^{(2,4)} = -\Delta S_{CDT}^{(4,2)} = 2\lambda$, and the gauge configuration is modified substantially, by the introduction or the removal of a central plaquette of length four, which is indicated as Π'_0 in Figure 13; at the same time, the length and composition of plaquettes $\Pi_{2 \leq i \leq 4}$ is changed as well.

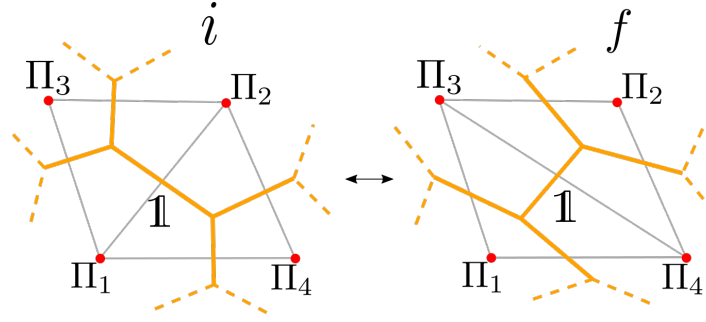


Fig. 12 Sketch of a $(2, 2)$ move. The link dual to the flipped edge is gauge fixed to the identity before the move, so that the 4 involved plaquettes keep the same value after the move. However, their contribution to the action does change, because of the modification in the coordination number of the four involved vertices.

The main new difficulty with respect to the $(2, 2)$ move is that, since plaquettes are gauge invariant objects, the appearance of the new plaquette cannot be masked completely by gauge fixing. Indeed, gauge transformations can set to the identity $\mathbb{1}$ at most three out of four links of the central plaquette Π'_0 , shifting all the physical content in the remaining one. Therefore, during the move, one has to draw at least one new gauge variable (or destroy it) with a non-trivial distribution, and this must be done properly, i.e. respecting detailed balance.

Let us consider for instance the $(2, 4)$ move. A necessary condition to implement detailed balance is that we can clearly identify pairs of states going into each other under the action of the move and of its inverse. Therefore, while the starting link dual to the two simplices involved in the move can be safely gauge fixed to the identity, the new plaquette, hence the new link U' in Figure 13, cannot, since in the corresponding inverse $(4, 2)$ move, in which it is destroyed, it will have in general a non-trivial starting value, drawn from the equilibrium distribution of gauge fields in the target triangulation.

Therefore, the $(2, 4)$ involves the extraction of a new link variable U' , which then also modifies the value of the plaquette Π'_2 . That can be done in various ways, with the condition that detailed balance be eventually satisfied by the final Metropolis-Hastings acceptance step. However, the most natural choice, which simplifies the final step and improves acceptance, is to draw U' from the heat-bath distribution in the target configuration, i.e. that corresponding to the force $F = \mathbb{1}/4 + X_2/n'_2$. For more details, we refer the reader to Ref. [39].

3.2.2 Perspectives for higher dimensions

In principle, the approach followed for the two-dimensional case can be extended to higher dimensions. However, the discussion reported above for the $(2, 4)$ and $(4, 2)$ moves clarifies what kind of difficulties may emerge. Let us consider, for example,

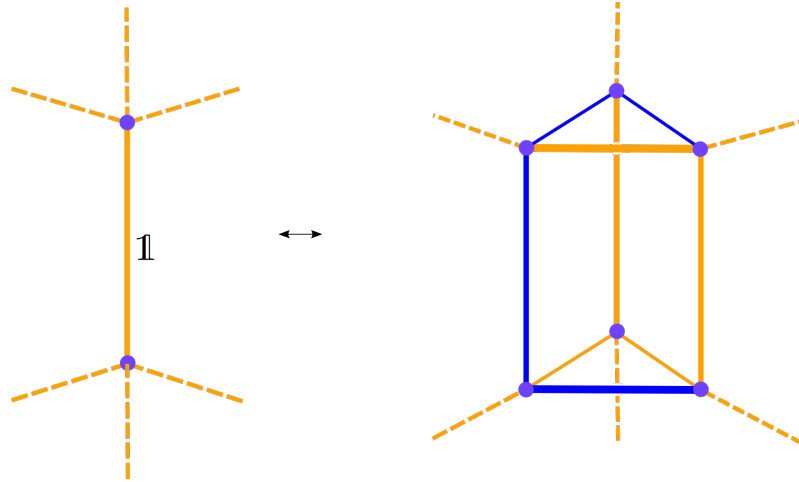


Fig. 14 Sketch of a possible implementation of the (2, 6) and (6, 2) moves on a three-dimensional causal triangulation, where 4 dynamical link variables (in blue) remain dynamical after gauge fixing; orange links show links gauge fixed to identity.

3.3 Gauge Fields on Dynamical Triangulations at work

In this Section we discuss some numerical results from simulations of 2D CDT coupled to Yang-Mills theories, considering both the $U(1)$ and $SU(2)$ gauge group. A detailed account of such results can be found in Ref. [39], here we only focus on a few aspects, which could be of particular interest when algorithms for higher dimensions will be available.

The first aspect regards how the critical behavior of the pure gravity theory is modified by the presence of gauge fields. This is of course relevant to the search for a critical point where a renormalized theory of quantum gravity could eventually be defined, since the coupling to other fields, either matter or gauge, modifies the renormalization group flow. As we will discuss, the two-dimensional case is somewhat trivial in this respect, since the coupling to gauge fields just renormalizes the cosmological constant and shifts its critical value, leaving critical indices unchanged.

As a second aspect, we consider the definition and behavior of gauge observables in the fluctuating space-time geometry. Among various possible gauge invariant quantities (see Ref. [39] for a more detailed discussion), we focus our attention here on observables related to the topology of gauge fields, in particular on the so-called winding number (or topological charge): this quantity classifies the possible mappings of the gauge group onto the space-time manifold, therefore it could be particularly interesting in a situation in which the latter is not fixed but instead fluctuating.

Before starting the discussion of results, let us briefly recap the main features of our simulations. The parameters entering the discretized theory are the bare cosmological constant λ , see Eq. (34), and the inverse gauge coupling $\beta \propto 1/g^2$,

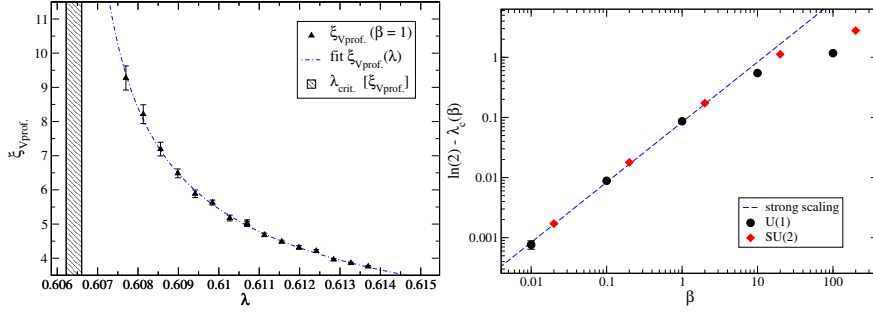


Fig. 15 Left: determination of $\xi_{V\text{prof.}}$ as a function of λ for the $U(1)$ gauge group at $\beta = 1$, together with the results of a fit to a power law behavior as in Eq. (36). Right: Critical values of λ for $U(1)$ and $SU(2)$ as a function of β ; the dashed line represents the strong coupling expansion prediction discussed in the text.

see Eq. (33), which differs from standard definitions used in lattice gauge theories by a proportionality factor, related to the bone coordination numbers n_b and to the fact that the reference flat discretization is hexagonal, rather than square, lattice. A further parameter is the number of temporal slices N_t , which is fixed, while the spatial extension of each slice is dynamical. The overall imposed topology is that of a torus, with periodic boundary conditions in the temporal and spatial directions: because of the Gauss-Bonnet theorem in two-dimensions, which implies a globally flat geometry, i.e. the condition $\langle n_b \rangle = 6$ holds for all sampled triangulations.

3.3.1 Critical behaviour

The pure gravity theory undergoes a continuous transition for a critical cosmological parameter $\lambda_c = \log(2)$. As the critical point is approached from above, one observes a divergence both of the average total volume $\langle V \rangle$ of the triangulation and of the length $\xi_{V\text{prof.}}$ describing the large distance behaviour of the correlation between the spatial extensions of pairs of different time slices, i.e. the two-point function of the so-called volume profile. The critical behaviour is described in terms of two critical indices ν and μ :

$$\langle V \rangle \propto (\lambda - \lambda_c)^{-\mu}, \quad \xi_{V\text{prof.}} \propto (\lambda - \lambda_c)^{-\nu}. \quad (36)$$

Such scaling laws are expected to hold sufficiently close to λ_c , i.e. in the so-called scaling window; results of Ref. [39] show that the scaling window for $\xi_{V\text{prof.}}$ is somewhat larger than that for $\langle V \rangle$.

The addition of gauge fields is not expected to lead to a significant modification of the critical behaviour. Indeed, it is known that two-dimensional gauge fields can be easily integrated away [43, 44, 45]. Nevertheless, on a curved geometry one is left with a non-trivial contribution, depending on the coordination numbers n_b , which could modify the behavior of gravity observables.

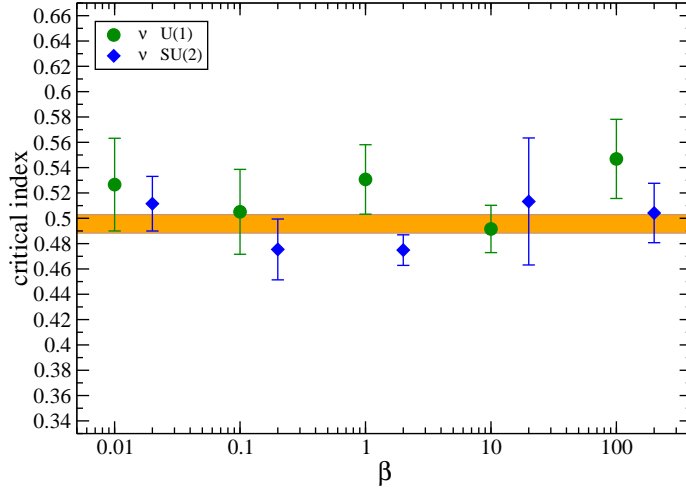


Fig. 16 Critical index ν , as a function of the bare gauge coupling β , for both explored gauge groups. The horizontal bands is the result of a best fit to constant value.

In Fig. 15 we report the behaviour of the correlation length as a function of λ for $\beta = 1$ and the $U(1)$ gauge group: results can still be nicely fitted according the scaling ansatz of Eq. (36), however with a different λ_c compared to the pure gravity case. The critical values of λ obtained for $U(1)$ and $SU(2)$ are reported in the same figure as a function of β , together with an analytical prediction based on a strong coupling expansion of the gauge theory, i.e. a series expansion in β [39].

Despite the change in the critical coupling, no appreciable change is observed, within errors, for the critical indices, as can be appreciated from Figure 16, where the values of ν obtained for different β and gauge groups are reported. To confirm the apparent stability of ν , we have performed a global fit of all values to a constant, obtaining $\nu = 0.496(7)$ ($\chi^2/\text{dof} = 9.1/9$). We notice that this value is compatible with a mean field critical index $1/2$.

These observations suggest that, in the two dimensional case, the presence of gauge fields modifies gravity just by an additive renormalization of the cosmological constant. The fact that local fluctuations of n_b are not relevant could be explained by the seemingly mean field behaviour. Of course, the situation could be quite different in higher dimensions.

As a final comment, it is clear that approaching λ_c at fixed inverse gauge coupling β is not enough to define a proper continuum limit for the whole theory. One should tune also β so that gauge-related correlation lengths diverge at the same time: in two space-time dimensions this is usually achieved as $\beta \rightarrow \infty$, with an asymptotic scaling of gauge correlation lengths proportional to $\sqrt{\beta}$.

3.3.2 Gauge topology

In two space-time dimensions, a topological classification of gauge configurations applies only to the case of $U(1)$ gauge group. In this case, the topological charge Q , or winding number, amounts to the total flux of the gauge field strength across the space-time manifold: gauge configurations with a non-integer topological charge are completely suppressed from the path-integral if the manifold is compact (like in our case, since we are on a torus), or if vanishing conditions at infinity are imposed on the field strength, so that relevant contributions to the path integral can be classified according to integer values of Q .

The very concept of homotopy classes is lost on a discrete space-time, but is recovered as the continuum limit is approached. A side effect of that, however, is the fact that, as the inverse gauge coupling β grows, standard updating algorithms become extremely inefficient in moving from one topological sector to the other, so that ergodicity is lost: this problem is usually known as topological freezing and affects standard simulations of lattice gauge theories [46, 47, 48, 49].

Within our formulation it is relatively easy to define an integer valued topological charge even on the discretized manifold

$$Q \equiv \frac{1}{2\pi} \sum_{b \in \mathcal{T}^{(d-2)}} \arg[\text{Tr}(\Pi_b)], \quad (37)$$

where Π_b is the plaquette around vertex b , and the argument function $\arg z$ returns values in $(-\pi, \pi]$.

In the following we discuss briefly results obtained for Q and for the so-called topological susceptibility $\chi \equiv \langle Q^2 \rangle / V$, comparing results from numerical simulations on a triangulation with fixed geometry, corresponding in particular to a flat torus, with those from dynamical simulations in which the geometry is updated as well. To start with, in Figure 17 we compare the Monte Carlo histories of Q obtained in the two cases for $\beta = 60$ and $\beta = 70$. In order to make the comparison meaningful, we tuned λ so has to have an average volume $\langle V \rangle$ equal to the volume used for the fixed geometry case.

Topological freezing emerges quite clearly in static simulations, indeed Q is fully frozen at $\beta = 70$; the interesting result is that, on the contrary, no freezing at all is observed in the dynamical case. We have checked that this phenomenon is induced by the typical roughness of the triangulation, rather than by its dynamical change during the Monte-Carlo evolution (see Ref. [39] for details). A possible explanation of this substantial improvement in the decorrelation of Q could be searched in the existence of regions with a large negative curvature (i.e., of vertices with a large coordination number n_b), where large fluctuations in the local flux of the field strength across the manifold are possible, with a limited expense in terms of the pure gauge action. It is reasonable to guess that this feature could extend to the higher dimensional case as well.

To conclude, in Figure 18 we show results obtained for the topological susceptibility (times β), comparing again the flat static and the dynamical case. We stress that,

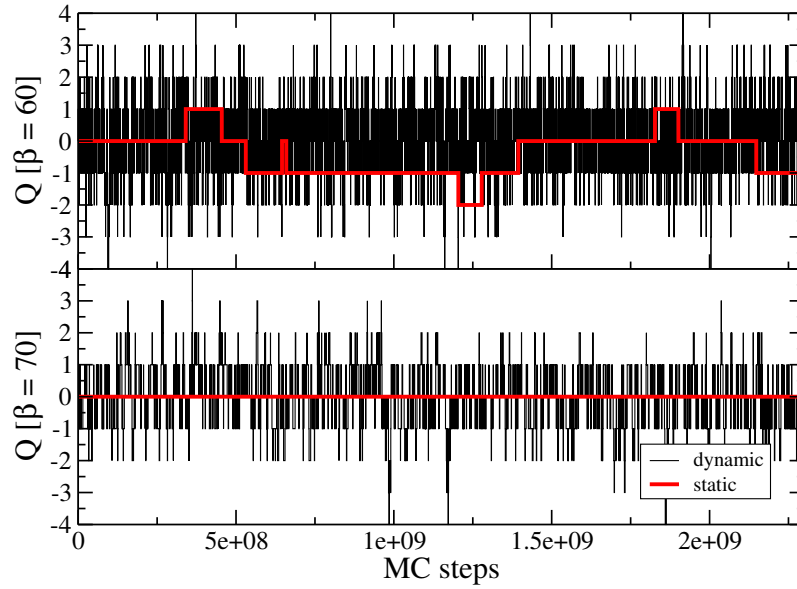


Fig. 17 Comparison of the Monte-Carlo histories of Q for the dynamic and static (flat) simulations with a comparable total volume $\langle V \rangle = 800$ and for two different inverse gauge couplings, $\beta = 60$ and $\beta = 70$.

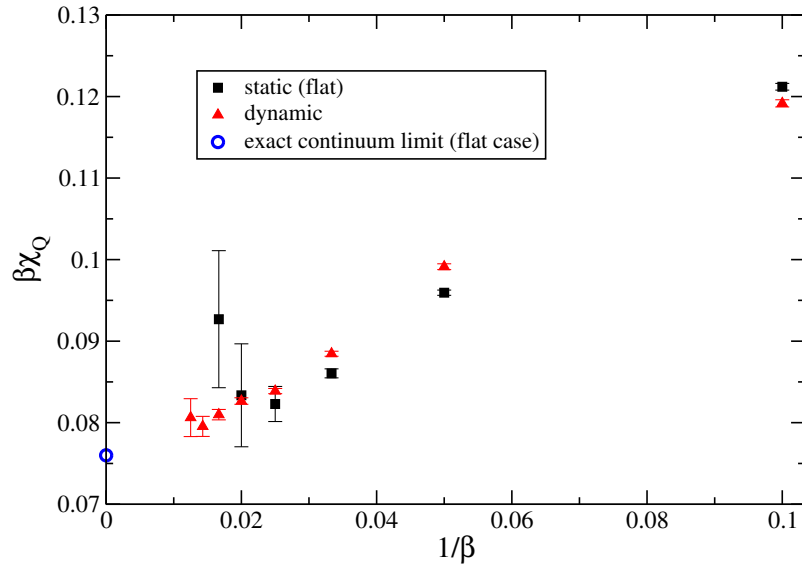


Fig. 18 Comparison of the topological susceptibilities $\langle Q^2/V \rangle$ obtained for the static (flat) and dynamic simulations at average volume $V = 800$.

in the dynamical case, an ambiguity emerges in the definition of χ , since the total volume itself fluctuates; our prescription is to define $\chi_Q \equiv \langle \frac{Q^2}{V} \rangle$, i.e., volume fluctuations are taken into account and included in one single average. Slight differences are observed at finite β , however, the improved decorrelation of Q in the dynamical case allows to obtain accurate results even at large values of β . Assuming $1/\beta$ corrections and considering only data with $\beta > 30$, we have tried to extract a continuum extrapolation (however, at fixed gravity coupling) obtaining $\beta\chi_Q = 0.0758(14)$ with a reduced chi-squared $\chi^2/\text{dof} = 1.6/3$: such result is in good agreement with the prediction for the flat continuum theory [45], $\beta\chi_Q = 3/(4\pi^2) \simeq 0.075991$, where we have taken into account an additional factor 6 in our definition of β .

4 Summary

This Chapter has been devoted to a few recent developments regarding the CDT approach to Quantum Gravity. As a first topic, in Section 2 we have discussed the need for new physical quantities characterizing the CDT phase diagram, focusing on spectral observables. We showed how information about the effective dimension at large scales and the characteristic scales of ensembles of geometries can be extracted from the spectrum, and discussed another possible discretization. However, there is still much to be investigated in the form of analysis of the properties of eigenvectors, such as their localization properties or a coarse-graining procedure for local observables by spectral projection in the eigenspace corresponding to the lowest part of the spectrum.

As a second topic, we have discussed how the CDT approach could be enlarged to include a minimal coupling to Abelian and non-Abelian gauge fields. While the general formulation is clear, present algorithms limit the exploration to the two-dimensional case. As a preliminary step, which is possible already with available algorithms, one could perform numerical simulations of gauge theories on fixed triangulations sampled via pure gravity CDT simulations: that would not give any information on the feedback of gauge fields on gravity, however could reveal interesting aspects about the influence of the underlying space-time geometry on gauge field dynamics.

References

1. J. Ambjørn, “(Causal) Dynamical Triangulations: a Regularization of Quantum Gravity”, Chapter 1 of the Section “Causal Dynamical Triangulations” of the “Handbook of Quantum Gravity” (Eds. C. Bambi, L. Modesto and I.L. Shapiro, Springer Singapore, expected in 2023).
2. J. Gizbert-Studnicki, “Semiclassical and Continuum Limits of Four-Dimensional CDT”, Chapter 10 of the Section “Causal Dynamical Triangulations” of the “Handbook of Quantum Gravity” (Eds. C. Bambi, L. Modesto and I.L. Shapiro, Springer Singapore, expected in 2023).

3. M. Reuter, F. Wolter, M. Shenton and M. Niethammer, "Laplace–Beltrami Eigenvalues and Topological Features of Eigenfunctions for Statistical Shape Analysis," *Computer-Aided Design* **41** no.10, 739 (2009)
4. M. Reuter, F. Wolter, M. Shenton and M. Niethammer, *Computer-Aided Design* **38** no.4, 342 (2006)
5. M. Belkin and P. Niyogi, "Laplacian eigenmaps and spectral techniques for embedding and clustering," In *Proceedings of NIPS'01* (2001) 585–591.
6. D.V. Vassilevich, "Heat kernel expansion: user's manual", *Phys. Rept.* **388**, 5 (2003).
7. P. W. Anderson, "Absence of Diffusion in Certain Random Lattices" *Phys. Rev.* **109** (1958), 1492-1505
8. L. Ujfalusi, M. Giordano, F. Pittler, T. G. Kovacs and I. Varga, "Anderson transition and multifractals in the spectrum of the Dirac operator of Quantum Chromodynamics at high temperature," *Phys. Rev. D* **92** (2015) no.9, 094513 [arXiv:1507.02162 [cond-mat.dis-nn]].
9. D. ben-Avraham and S. Havlin, "Diffusion and Reactions in Fractals and Disordered Systems", Cambridge University Press (2005)
10. J. Ambjørn, D. Boulatov, J.L. Nielsen, J. Rolf and Y. Watabiki, "The spectral dimension of 2-D quantum gravity", *JHEP* **02** (1998) 010 arXiv:hep-th/9801099.
11. J. Ambjørn, J. Jurkiewicz and R. Loll, "The Spectral Dimension of the Universe is Scale Dependent", *Phys. Rev. Lett.* **95** (2005) 171301 arXiv:hep-th/0505113
12. J. Ambjorn, J. Jurkiewicz and R. Loll, "Reconstructing the universe" *Phys. Rev. D* **72** (2005) 064014
13. H. P. McKean, I. Singer, "Curvature and the eigenvalues of the Laplacian", *J. Differential Geometry* **1** no.1, 43 (1967)
14. H. Weyl, *Nachr. Königl. Ges. Wiss. Göttingen*, 110–117 (1911).
15. V. Ivrii, "100 years of Weyl's law", *Bulletin of Mathematical Sciences* **6** (2016) no.3, 379–452 [arXiv:1608.03963v2 [math.SP]].
16. G. Clemente and M. D'Elia, "Spectrum of the Laplace–Beltrami operator and the phase structure of causal dynamical triangulations", *Phys. Rev. D* **97** (2018) 124022 [arXiv:1804.02294 [hep-th]].
17. J. Cheeger, "A lower bound for the smallest eigenvalue of the Laplacian," *Problems in analysis* (Sympos. in honor of Salomon Bochner, Princeton Univ., Princeton, N.J., 1969), pp. 195–199. Princeton Univ. Press, Princeton, N.J., 1970.
18. J. Ambjorn, S. Jordan, J. Jurkiewicz and R. Loll, "A Second-order phase transition in CDT", *Phys. Rev. Lett.* **107** (2011) 211303 [arXiv:1108.3932 [hep-th]].
19. J. Ambjorn, S. Jordan, J. Jurkiewicz and R. Loll, "Second- and First-Order Phase Transitions in CDT," *Phys. Rev. D* **85** (2012) 124044 [arXiv:1205.1229 [hep-th]].
20. J. Ambjørn, J. Gizbert-Studnicki, A. Görlich, J. Jurkiewicz, N. Klitgaard and R. Loll, "Characteristics of the new phase in CDT," *Eur. Phys. J. C* **77** (2017) 152 [arXiv:1610.05245 [hep-th]].
21. J. Ambjorn, D. Coumbe, J. Gizbert-Studnicki, A. Gorlich and J. Jurkiewicz, "New higher-order transition in causal dynamical triangulations," *Phys. Rev. D* **95** (2017) 124029 [arXiv:1704.04373 [hep-lat]].
22. J. Ambjorn, J. Jurkiewicz and R. Loll, *Phys. Rev. Lett.* **93** (2004) 131301 [hep-th/0404156].
23. M. Reitz, D. Németh, D. Rajbhandari, A. Görlich and J. Gizbert-Studnicki, "Generalised spectral dimensions in non-perturbative quantum gravity," [arXiv:2207.05117 [gr-qc]].
24. F. Caceffo and G. Clemente, "Spectral analysis of causal dynamical triangulations via finite element method," *Phys. Rev. D* **107** (2023) no.7, 074501 [arXiv:2010.07179 [hep-lat]].
25. G. Allaire and A. Craig, "Numerical Analysis and Optimization," Oxford University Press (2007)
26. T.J.R. Hughes, "The Finite Element Method: Linear Static and Dynamic Finite Element Analysis", Dover Publications (2000)
27. G. Strang and G. Fix, "An Analysis of the Finite Element Method", Wellesley-Cambridge Press (2008)
28. O.C. Zienkiewicz, R.L. Taylor and J.Z. Zhu, "The Finite Element Method: its Basis and Fundamentals", Butterworth-Heinemann (2013)

29. B. Szabó and I. Babuska, “Finite Element Analysis”, Wiley-Interscience (1991)
30. G. Clemente, M. D’Elia and A. Ferraro, “Running scales in causal dynamical triangulations,” *Phys. Rev. D* **99** (2019) no.11, 114506 [arXiv:1903.00430 [hep-th]].
31. G. Clemente, M. D’Elia and A. Ferraro, “Spectral Methods in Causal Dynamical Triangulations” PoS **Lattice2019** 116 arXiv:1912.11311 [hep-lat]
32. K. G. Wilson, “Confinement of Quarks,” *Phys. Rev. D* **10** (1974), 2445-2459
33. T. Regge, “General Relativity Without Coordinates,” *Nuovo Cim.* **19** (1961) 558.
34. J. Ambjorn, A. Goerlich, J. Jurkiewicz and R. Loll, “Nonperturbative Quantum Gravity,” *Phys. Rept.* **519** (2012) 127 [arXiv:1203.3591 [hep-th]].
35. N. Metropolis, A. W. Rosenbluth, M. N. Rosenbluth, A. H. Teller and E. Teller, “Equation of state calculations by fast computing machines,” *J. Chem. Phys.* **21** (1953) 1087
36. W. K. Hastings, “Monte Carlo Sampling Methods Using Markov Chains and Their Applications,” *Biometrika* **57** (1970) 97
37. J.W. Alexander, “The combinatorial theory of complexes,” *Ann. Mat.* **31** (1931) 292.
38. J. Ambjørn, J. Jurkiewicz and R. Loll, “Lorentzian and Euclidean Quantum Gravity — Analytical and Numerical Results,” *NATO Sci. Ser. C* **556** (2000) 381 [arXiv:hep-th/0001124 [hep-th]].
39. A. Candido, G. Clemente, M. D’Elia and F. Rottoli, “Compact gauge fields on Causal Dynamical Triangulations: a 2D case study,” *JHEP* **04** (2021), 184 [arXiv:2010.15714 [hep-lat]].
40. M. Creutz, “Monte Carlo Study of Quantized SU(2) Gauge Theory,” *Phys. Rev. D* **21** (1980) 2308
41. A. D. Kennedy and B. J. Pendleton, “Improved Heat Bath Method for Monte Carlo Calculations in Lattice Gauge Theories,” *Phys. Lett. B* **156** (1985) 393
42. N. Cabibbo and E. Marinari, “A New Method for Updating SU(N) Matrices in Computer Simulations of Gauge Theories,” *Phys. Lett. B* **119** (1982), 387-390 doi:10.1016/0370-2693(82)90696-7
43. J. Ambjorn and A. Ipsen, “Two-dimensional causal dynamical triangulations with gauge fields,” *Phys. Rev. D* **88** (2013) no.6, 067502 [arXiv:1305.3148 [hep-th]].
44. C. Cao, M. van Caspel and A. R. Zhitnitsky, “Topological Casimir effect in Maxwell Electrodynamics on a Compact Manifold,” *Phys. Rev. D* **87** (2013) 105012 [arXiv:1301.1706 [hep-th]].
45. C. Bonati and P. Rossi, “Topological susceptibility of two-dimensional $U(N)$ gauge theories,” *Phys. Rev. D* **99** (2019) 054503 [arXiv:1901.09830 [hep-lat]].
46. B. Alles, G. Boyd, M. D’Elia, A. Di Giacomo and E. Vicari, “Hybrid Monte Carlo and topological modes of full QCD,” *Phys. Lett. B* **389** (1996) 107 [arXiv:hep-lat/9607049 [hep-lat]].
47. L. Del Debbio, G. M. Manca and E. Vicari, “Critical slowing down of topological modes,” *Phys. Lett. B* **594** (2004) 315 [arXiv:hep-lat/0403001 [hep-lat]].
48. M. Luscher and S. Schaefer, “Lattice QCD without topology barriers,” *JHEP* **07** (2011) 036 [arXiv:1105.4749 [hep-lat]].
49. C. Bonati and M. D’Elia, “Topological critical slowing down: variations on a toy model,” *Phys. Rev. E* **98** (2018) 013308 [arXiv:1709.10034 [hep-lat]].